AWARD NUMBER: W81XWH-15-1-0009

TITLE: Photovoltaic Retinal Prosthesis for Restoring Sight to Patients Blinded by Retinal Injury or Degeneration

PRINCIPAL INVESTIGATOR: Prof. Daniel Palanker

CONTRACTING ORGANIZATION: Leland Stanford Junior University
Palo Alto, CA 94304

REPORT DATE: April 2018

TYPE OF REPORT: Final

PREPARED FOR: U.S. Army Medical Research and Materiel Command
Fort Detrick, Maryland 21702-5012

REPORT DOCUMENTATION PAGE

Form Approved
OMB No. 0704-0188

1. REPORT DATE	2. REPORT TYPE	3. DATES COVERED
April 2018	Final	1 Feb 2015 - 31 Jan 2018

4. TITLE AND SUBTITLE
Photovoltaic Retinal Prosthesis for Restoring Sight to Patients Blinded by Retinal Injury or Degeneration

5a. CONTRACT NUMBER

5b. GRANT NUMBER
W81XWH-15-1-0009

5c. PROGRAM ELEMENT NUMBER

6. AUTHOR(S)
Prof. Daniel Palanker

E-Mail: palanker@stanford.edu

5d. PROJECT NUMBER

5e. TASK NUMBER

5f. WORK UNIT NUMBER

7. PERFORMING ORGANIZATION NAME(S) AND ADDRESS(ES)

Leland Stanford Junior University
452 Lomita Mall, Room 135, Astrophysics Building,
Stanford, CA 94305-4085

8. PERFORMING ORGANIZATION REPORT NUMBER

9. SPONSORING / MONITORING AGENCY NAME(S) AND ADDRESS(ES)

U.S. Army Medical Research and Materiel Command
Fort Detrick, Maryland 21702-5012

10. SPONSOR/MONITOR'S ACRONYM(S)

11. SPONSOR/MONITOR'S REPORT NUMBER(S)

12. DISTRIBUTION / AVAILABILITY STATEMENT

Approved for Public Release; Distribution Unlimited

13. SUPPLEMENTARY NOTES

14. ABSTRACT: Traumatic retinopathy and retinal degeneration lead to blindness due to loss of photoreceptors. Visual information can be reintroduced into the retina by patterned electrical stimulation of the remaining inner retinal neurons. Photovoltaic subretinal prosthesis directly converts light into pulsed electric current in each pixel, stimulating the nearby neurons. Images captured by the goggles-mounted camera are projected onto retina in augmented-reality goggles using pulsed near-infrared (~880nm) light. We prepared this technology for a clinical trial, including optimization of the photovoltaic array, addition of the biocompatible protective coating for long-term implantation, fabrication of the video goggles with a camera, and image processing software.

After technology transfer to our partner company, Pixium Vision, the first clinical trial started in 2018. To date, 3 photovoltaic arrays of 2x2mm in size and 30µm in thickness, with 100µm pixels have been implanted in patients with geographic atrophy. All patients perceive white-yellow patterns with adjustable brightness, in retinotopically correct locations. Majority of them correctly differentiate simple objects and recognize patterns, such as bars at different orientations, with spatial resolution up to the limits of the implant. These results indicate that further development of smaller pixels should provide higher resolution and enable even more functional restoration of sight.

15. SUBJECT TERMS

None provided

16. SECURITY CLASSIFICATION OF:			17. LIMITATION OF ABSTRACT	18. NUMBER OF PAGES	19a. NAME OF RESPONSIBLE PERSON
a. REPORT	b. ABSTRACT	c. THIS PAGE			USAMRMC
Unclassified	Unclassified	Unclassified	Unclassified	20	19b. TELEPHONE NUMBER *(include area code)*

Table of Contents

Page

Introduction

Ocular trauma can result in traumatic retinopathy, which, like retinal degeneration, leads to blindness due to loss of photoreceptors. Visual information can be reintroduced into the retina by patterned electrical stimulation of the remaining inner retinal neurons. Photovoltaic subretinal prosthesis directly converts light into pulsed electric current in each pixel, stimulating the nearby neurons. Images captured by the head-mounted camera are projected onto retina by video goggles using pulsed near-infrared (~880nm) light. Preparation of this technology for clinical trial requires optimization of the photovoltaic array, addition of the biocompatible protective coating for long-term implantation in human patients, fabrication of the video goggles with a camera, and image processing software. In particular, we (1) Developed and tested the SiC protective biocompatible coating for the implant. (2) Optimized the pixel configuration to maximize its performance, including the light-to-current conversion, dynamic range, maximum repetition rate, minimum cross-talk and minimum pixel size. (3) Developed the near-infrared pulsed video goggles and the image processing software.

Results

The results of our research are presented below, listed by specific tasks:

Major Task 1: Development and testing of the SiC protective biocompatible coating for the implant

To protect subretinal photovoltaic array from erosion, we developed silicon carbide (SiC) protective coating, and evaluated its degradation in accelerated aging in-vitro as well as in a year-long follow-up in-vivo. For the latter, we characterized degradation of the implant by optical and scanning electron microscopy (SEM) after explantation. We also measured the dissolution rates of SiC, SiN_x and thermal SiO_2 in accelerated soaking tests to compare stability of those dielectric materials. We analyzed the defects in SiC films, and defined the optimal thickness of SiC layer for reliable protection of the chronic implants.

SiC was deposited by plasma-enhanced chemical vapor deposition (PECVD) at EIC Laboratories, Inc. (Norwood, MA). The precursors were SiH_4 and CH_4 (1:3 ratio of SiH_4/CH_4) in an Ar carrier gas. The deposition temperature was 325°C at a pressure of 800mTorr and an RF power frequency of 13.56MHz. The SiN_x used in dissolution rate tests was deposited by PECVD at the Stanford Nanofabrication Facility (SNF) using Surface Technology Systems (STS) PECVD. The precursors were SiH_4 and NH_3 (40:33.5 ratio of SiH_4/NH_3) at a deposition temperature of 350°C and pressure of 650 mTorr. Dual frequency (13.56MHz and 187.5kHz) deposition was used. SiN_x was deposited as the top surface coating of retinal prostheses by PECVD at SNF (Plasma-Therm Shuttlelock SLR-730-PECVD). This tool used a capacitive-coupled plasma with 13.56MHz RF power. Precursors were SiH_4 and NH_3 (5:3 ratio of SiH_4/NH_3), with He and N_2 carrier gases. The deposition temperature was 350°C at a pressure of 950mTorr. SiO_2 was grown by wet thermal oxidation in a resistance-heated oxidation furnace at 1000°C.

Each of the six Type I retinal prostheses (three with SiC coating and three without) were implanted sub-retinally in a different rat (six rats in total). The implantation technique was similar to the one previously reported by our group and performed in agreement with Stanford University institutional guidelines and the Statement for the Use of Animals in Ophthalmic and Vision Research. After a period of time (from 4 months to 1 year), implants were extracted from the tissue and cleaned in an enzyme solution (Tergazyme, 1%) for one day, and then further cleaned with deionized water and isopropyl alcohol (IPA). Explanted devices were examined with optical and scanning electron microscopy. Some

devices were sputter coated with a thin layer of metal (~10nm) to improve the SEM imaging by reducing the charging effects. It was not always possible to compare the same device and the same pixel before and after the implantation due to randomness of the defect locations. However, each optical and SEM image is representative of the type of implant in terms of the device structure and changes after the implantation.

Implants without SiC coating degraded significantly, with visible signs of erosion becoming evident after 4-month sub-retinal implantation. SiN_x layer was completely dissolved on all pixels and devices, which was evident from the color change of the devices after implantation. Polysilicon in the trench also significantly degraded (Figure 1).

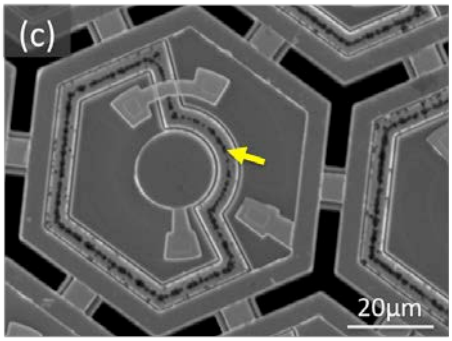

Figure 1. **SEM of retinal prostheses without SiC coating 4 months after implantation.** Polysilicon in the trench is degraded, as pointed by the arrow.

For comparison, three devices with 240nm of SiC coating were implanted in three different rats for 4 months. One implant did not show any visible degradation under the optical microscope (Figure 2). Two other implants had minor isolated defect points, visible as small patches of color change near the middle of the polysilicon-filled trenches compared to the image before implantation. These defects were seen on 51 out of 142 pixels on one device, and 41 out of 142 on another. The patches of color changes indicate the presence of defects in the SiC films near the middle of the polysilicon-filled trenches, which allowed dissolution of the underlying SiN_x.

SiC also exhibited excellent stability during accelerated aging in-vitro. After more than 16 weeks in saline at 87°C, they showed neither visible degradation nor quantifiable dissolution. This result explains why SiC-coated devices were so stable *in vivo*. Thermally grown SiO_2 dissolved very slowly but steadily at 1.04±0.08A/day in saline at 87°C (Figure 5b). Thus a SiO_2 coating of 70nm would last for ~700 days under the accelerated aging conditions, corresponding to tens of years *in vivo*. This explains why the single-crystal silicon part of the implant did not degrade *in vivo* after 1 year, with 70-80nm of SiO_2 covering it.

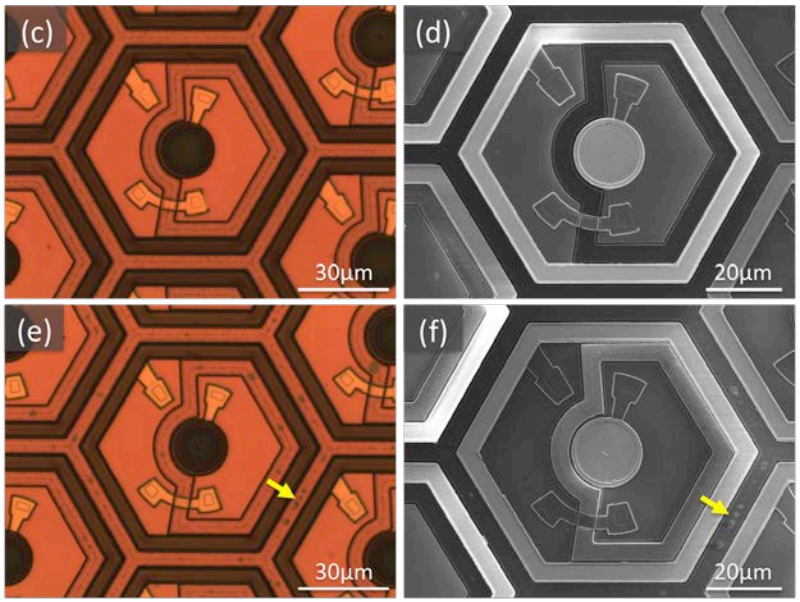

Figure 2. **Retinal prostheses with 240nm SiC coating 4 months after sub-retinal implantation in a rat eye**. Pixels shown in (c, d) exhibit no signs of degradation, while in (e, f) show small patches of color change in the middle of the polysilicon-filled trench (arrows), indicating defects in the SiC film.

In conclusion, significant degradation of unprotected photovoltaic retinal prostheses was found after 4-month implantation, especially in the polysilicon-filled trenches. PECVD SiC films were much more effective than SiN_x and SiO_2 coatings in protecting the devices *in vivo*. Accelerated aging tests did not change the thickness of SiC film after 112 days in saline at 87°C. The SiN_x coating was much less stable, and dissolved at 18.3±0.3nm/day at 87°C. Thermal SiO_2 grown at high temperature (1000°C) was more stable, but still dissolved very slowly at 1.04±0.08A/day at 87°C in saline. SiC films exhibited some defects on

complicated topography and rough surfaces. The defect density could be reduced or eliminated by smoothening the underlying surface or by increasing the SiC film thickness. Overall, PECVD SiC films have desirable properties as protective coatings for implantable electronics. A combination of thermal SiO_2 with a PECVD SiC film should be adequate for providing anti-reflective coating and protecting retinal prostheses for long-term use.

Major Task 2: Optimization of the pixel configuration to maximize its performance, such as light-to-current conversion efficiency, dynamic range, maximum repetition rate, and minimum cross-talk.

1. Verification of the photovoltaic implant performance by measurement of the contrast sensitivity of prosthetic vision ex-vivo

Introduction

We developed a completely wireless approach based on subretinally placed photodiode arrays, which photovoltaicly convert projected image into electric current flowing through the retina between the active and return electrode in each pixel to stimulate the nearby inner retinal neurons[1]. Images captured by the camera are processed and projected onto the retina from video goggles using near-infrared (NIR, 880-915nm) light to avoid photophobic and phototoxic effects of by bright illumination[1].

Previously we demonstrated retinal adaptation to high frequency (>20Hz) subretinal stimulation[1] as opposed to direct stimulation of ganglion cells, which can follow stimulation at rates exceeding 100Hz. Adaptation to subretinal stimulation is similar to flicker fusion occurring with normal vision at high frequencies, which allows continuous perception of movies composed of static frames. This feature is critical for prosthetic vision since electrical stimulation has to be pulsed in order to preserve charge balanced and thereby avoid irreversible electrochemical reactions at the electrode-electrolyte interface.

One of the important characteristics of vision in general, and of prosthetic vision in particular, is contrast sensitivity. With a carrier frequency above flicker fusion, contrast can be modulated by slow adjustments of either the amplitude or duration of the pulsed stimuli. In a previous *ex-vivo* study we measured the increase in spiking rate with increasing irradiance, and the corresponding contrast was about 60%, as opposed to 3% with natural vision in rodents[2]. However, these measurements did not quantify other changes in the RGCs firing patterns. Here we revisited the measurements of contrast sensitivity using a novel analysis of the firing patterns in prosthetic and natural vision, and demonstrate significantly higher contrast sensitivity[3].

Methods

Photovoltaic implants

The 1 and 2mm-wide arrays of 30μm in thickness with photovoltaic pixels of 70, 140 and 280μm in size were manufactured according to the previously described methods, except for reversal of the n- and p-doped regions to produce anodic-first pulses[4]. In these measurements, we used arrays of 1 mm in diameter with 70μm pixels.

Electrophysiological Recordings

A small piece of RCS or WT rat retina (~3mm x 3mm) was isolated and placed on a 512-electrode recording array (MEA) ganglion cell side down. The retina was constantly perfused with Ames' medium at 29.4 °C and bubbled with a mixture of 95% O2 and 5% C02. For assessment of prosthetic vision, a photovoltaic implant was placed on top of the retina, mimicking a subretinal placement *in-vivo.* We used a nylon mesh (~100um cell size) to lightly press the implant and retina onto the MEA to achieve good contact. The same procedures were undertaken for natural vision without the implant in place. Voltage waveforms were amplified and digitized with 20 kHz sampling frequency for each of the 512 electrodes on the MEA.[15]

For prosthetic vision, the 880nm diode laser coupled via a 400-μm multimode fiber was used for illumination. The beam exiting from the fiber was collimated, homogenized using a 2° divergence microlens array diffuser, and projected onto the implant via the camera port of an inverted microscope. The projection system was calibrated to deliver upto a maximum power of 8mW/mm^2 onto the sample. For single-pulse stimulation, 4-ms square NIR pulses were applied at 1 Hz repetition rate, and *n=120* trials were used to determine the RGC responses. For contrast sensitivity measurements, we used a carrier waveform consisting of 4-ms square NIR pulses applied at 20 Hz. Contrast steps were constructed by modulating the amplitude (peak power) with 0.5-second-long phase of 8mW/mm^2, followed by a 0.5-second-long phase of a chosen lower light intensity, and then return to 8mW/mm^2. We used *n=80* trials for every contrast step.

For natural vision, the image of a 15" CRT screen was optically reduced in size and projected onto the photoreceptor layer of a healthy retina through the camera port of the inverted microscope. Modulation of light intensity was performed with 0.5-second-long steps, similar to the envelop of prosthetic stimulation. In addition to full-field light intensity steps, we stimulated WT retinas with spatiotemporal monochromatic white noise using 70x70μm pixels refreshed every 33ms in order to differentiate between ON- and OFF-center RGC types.

Data Analysis

Raw recording traces from prosthetic stimulation were first subjected to electrical stimulation artifact removal. For every individual electrical pulse and electrode, we estimated the artifact by fitting a 7th-order polynomial to the data between 8.25 ms and 50 ms proceeding the onset of the pulse. The fitted polynomial was then subtracted from the raw voltage trace. Since an overly large artifact during the first 8.25 ms following the onset of pulse could not be removed, we replaced that portion with a randomly generated noise. As a result, action potentials (spikes) elicited during that period were discarded.

The artifact-subtracted traces were then used for spike detection and sorting using custom software described previously[4]. Spikes were defined as an event where the negative voltage deflection amplitude exceeded 3 times root-mean-squared noise on each electrode. We applied dimensionality reduction to the detected spike waveforms using principal component analysis, followed by expectation-maximization clustering. For each putative neuron, we calculated the electrophysiological image (EI) of the neuron - the average electrical signal measured on the whole multielectrode array when the neuron produced an action potential. It typically shows the soma location and axonal trajectory of the RGC. Neurons with abnormal EIs were excluded from our analysis. Responses of neurons to prosthetic stimulation were manually classified according to their raster response properties. For visible light stimulation, cells were classified as ON- and OFF-center types based on polarity of the first peak in the spike-triggered average (STAs) traces.

We used the Michelson definition for contrast $(I_{post} - I_{pre})/(I_{post} + I_{pre})$, where I_{pre} and I_{post} are the luminances (or peak irradiance for prosthetic stimulation) preceding or following the contrast step, respectively. To assess cellular response to prosthetic stimulation, we compared the distributions of spike rates 250 ms before and after a contrast step. The spike times were binned over 80 trials, and the resulting histograms were compared using the two-sample Kolmogorov-Smirnov test. Bin widths varying between 5 and 12.5 ms were compared and optimized to yield minimal *p*-values. For visible light stimulation, the activity of a cell subjected to 0.5% contrast was considered as the baseline spontaneous firing rate. Firing pattern of each RGC from 25 ms to 250 ms post-contrast step was compared to its baseline, using the same statistical method as for electrical stimulation. The first 25 ms was excluded because RGC activity was delayed due to the latency caused by the slow phototransduction process.

RGC responses to single-pulse electrical stimulation

To assess RGC responses to photovoltaic stimulation at various light intensities, we applied isolated 4-ms laser pulses over *n=120* trials to an implant gently pressed onto an RCS retina above the MEA. In P200 rats, four types of responses could be distinguished by their excitatory and inhibitory phases (Figure 1). Majority of cells (N=41/58) exhibited type 1 response (Figure 1A), and generally they were more abundant near the center of the implant. The most notable feature in this response type is the presence of two inhibitory phases at high irradiances, including a short-latency complete suppression of spontaneous firing, and a delayed long inhibition, which could last for 250 ms. The first inhibitory phase has a lower stimulation threshold than the proceeding peak. A considerable number of cells had similar responses, but did not feature the delayed inhibition. This could be attributed to the separation of the cell from the center of the implant, at which the electrical stimulation did not reach the inhibition threshold.

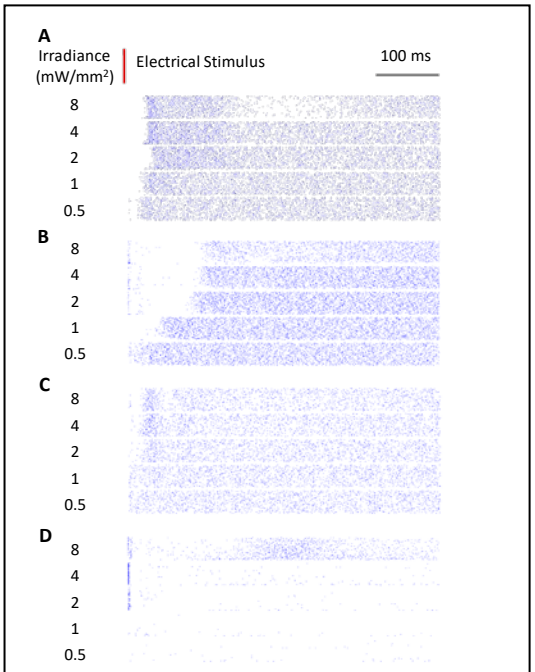

Figure 1. Four types of RGC responses to single pulse stimulation.

The signature of response type 2 (N=6/58, Figure 1B) was its short-latency long-duration inhibition that could extend up to 100 ms post-stimulus. The short latency peak appeared from intermediate irradiances (2 mW/mm^2). Since the data during the first 8.25 ms following the electrical pulse was discarded due to electrical artifact (see Methods), shorter latency responses could not be observed.

Response type 3 (N=5/58, Figure 1C) exhibited initial inhibition, followed by an excitatory peak. At high light intensities, a second period of inhibition and excitation can be observed. Oscillatory activity in the degenerate retina can be due to the amacrine cells[22], and this type of response may be a manifestation of these oscillations. It is not completely clear whether this response is a weak type 1 response superimposed on an oscillatory pattern, or a completely distinct phenomenon.

A very distinct response type could be found in cells with low spontaneous firing rate. This type (N=6/58, Figure 1D) has higher threshold than the other responses. At intermediate intensities, a short low-latency peak appears immediately after the blanking period. As the intensity increased further, long spread-out peak appeared, spanning from 150ms to 380ms. The peak time and duration resembles that of the second inhibition period in type 1 cells.

RGC responses to repetitive electrical stimulation

Cells responding to a 1 second burst of 4-ms NIR pulses repeated at 20 Hz were cross-identified using EIs obtained with their single-pulse stimulation, and their responses are shown in Figure 2. Due to artifact removal, 8.25-ms time intervals are excluded in every 50ms long cycle, creating empty vertical strips in the raster plot.

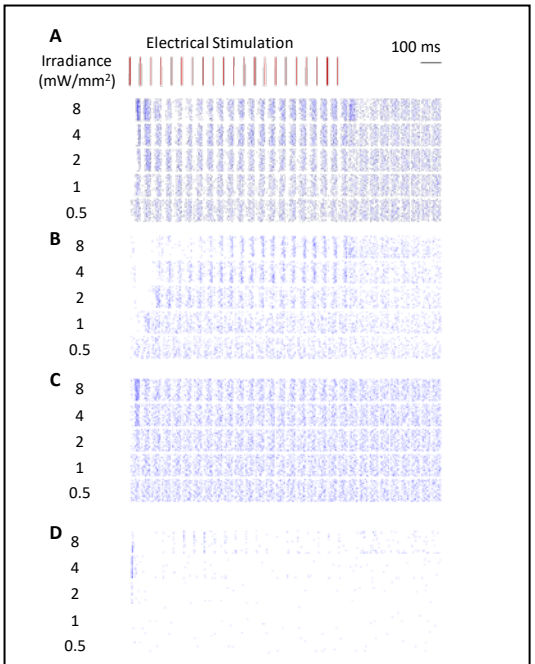

Figure 2. Four types of RGC responses to repetitive stimulation at 20 Hz.

In response type 1, the short latency inhibition occurred after every pulse at all measured irradiances. Excitatory responses appeared at irradiances above 2 mW/mm^2. Delayed transient inhibition occurs at 8 mW/mm^2, and the timing of maximal inhibition aligns with that observed during single-pulse stimulation. The long inhibition in response type 2 was mostly transient under fast repetitive stimulation. Type 3 cells showed strong response only on the first pulse, and very quickly adapted to the repetitive stimulus. Unlike type 1 and 2, the adapted state of these cells includes spiking rate similar to spontaneous firing, with only mild modulation by the periodic stimulus. Typically, this type of cell has higher stimulation thresholds than types 1 and 2. In type 4 cells, the first peak appeared immediately after the first pulse of the stimulus, and only at high irradiance it was repeated after every pulse during about half-a-second.

Contrast Sensitivity

To measure contrast sensitivity of a healthy retina, we projected full-field white light stimuli, varying the irradiance every second. Similar measurements were performed with photovoltaic stimulation of RCS retina, using 1-second-long bursts of 4-ms pulses at 20-Hz with variable intensity. Visual OFF cells responded to lowest levels of contrast (Figure 3). Previously, contrast sensitivity assessment ex-vivo[2] was based on increase in the spiking rate relative to spontaneous firing. To include other aspects of the retinal response, such as inhibitory behavior, we applied a new metric: comparing the spike rate distribution within 25 - 250 ms of a contrast step to spontaneous activity (2-sample K-S test). Low p value indicates the difference in temporal distribution of spiking within the two patterns. Under this metric, visual OFF cells ramp up rapidly from 0 to 3% contrast, and reach plateau above 5% contrast (Figure 3). The full width at half minimum (FWHM) in (1-*p*)-value for visual stimulation corresponded to 2.5% contrast.

Response to electrical stimulation steps had higher threshold and increased over a wider range (Figure 4A). The thresholds agree across different levels of degeneration. An OFF contrast step transitioned a cell from one adapted state to another faster than the ON step. For each contrast step, we compared the spike rate distribution 250 ms before and after the change in irradiance. Stimulation efficacy strongly depends on proximity of the implant to the retina. This effect is illustrated by the difference in contrast sensitivity between the two preparations with P200 RCS rats (Figure 4B). Prosthetic responses of degenerate retinas had significantly

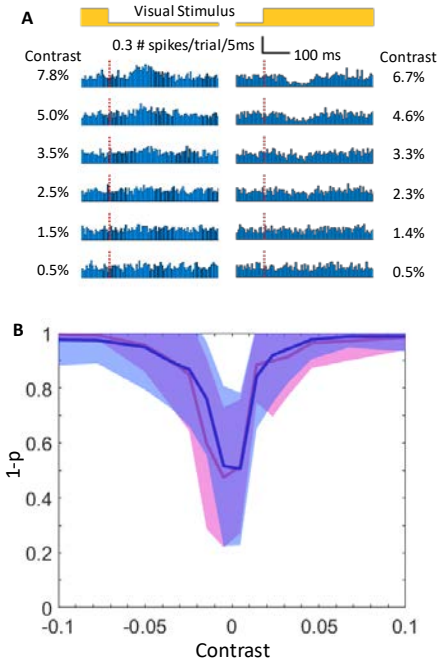

Figure 3. A. PSTH of a type-1 cell to ON and OFF visual contrast steps. **B**. Contrast sensitivity. The vertical width of each color band is +/- one sigma for each contrast level.

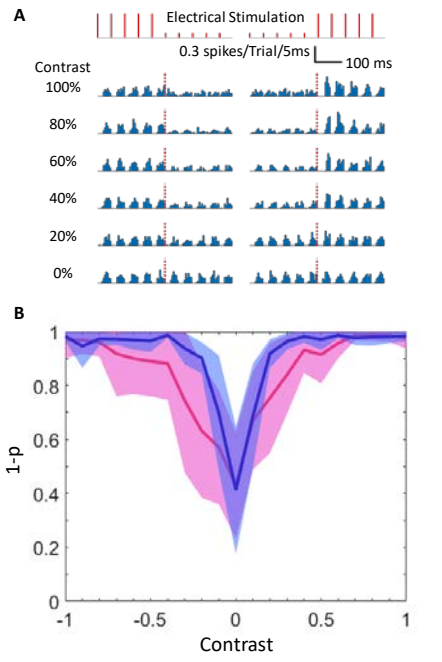

Figure 4. A. PSTH of a type-1 cell to ON and OFF electrical contrast steps. **B.** Contrast sensitivity with electrical stimulation.

lower contrast sensitivity than with natural vision: FWHM was 17%, and the (1-*p*) values at +17/-10% contrast in electrical stimulation corresponded to +/-2% contrast in visual stimulation, respectively.

2. Manufacturing of the optimized photovoltaic arrays with pixel sizes down to 40 μm

Network-mediated stimulation of the retina with subretinal implants allows preservation of several important features of natural vision, including flicker fusion at high frequencies (>20Hz), adaptation to static images, and non-linear summation of sub-units in receptive fields of RGCs, which enables high spatial resolution[1]. We have demonstrated that with 70μm pixels, prosthetic visual acuity in rats blinded by retinal degeneration matches the pixel pitch [1], and cortical responses are maintained for the life of animals (1-year post implantation).

After development of SiC protective coating to ensure long-term stability of the implant in-vivo[5], this technology is being transferred to Pixium Vision, a company which is preparing it for a clinical trial. Using arrays with 70μm pixels, we hope to achieve spatial resolution corresponding to 20/250 acuity.

Since the acuity matched the pixel pitch and stimulation thresholds were much lower than the ocular safety limits[4, 6], we are developing even smaller pixels, and plan to test the limits of prosthetic vision in animal models of retinal degeneration. Doubling the pixel density would enable spatial resolution corresponding to 20/120 visual acuity. This would make retinal prosthetics applicable not only to relatively few RP patients, but to millions of patients with loss of central vision due to late-stage AMD (geographic atrophy).

Methods and Results

The 5μm-wide open trenches between the pixels in our original design were essential for ex-vivo experiments on multi-electrode arrays since they enable diffusion of oxygen and nutrients to the retina sandwiched between the stimulating and recording arrays. However, experiments in-vivo demonstrated that implants without trenches are well tolerated in the animal since the inner retina is supplied by oxygen and nutrients via the retinal vasculature above the implant. Therefore, we eliminated these trenches and increased pixel density. In addition, each diode in the pixel was isolated by the surrounding 5μm-wide isolation trench. We now developed technology for producing 1μm-wide trenches filled with SiO_2 in 30 μm-thick silicon, corresponding to aspect ratio of 30:1 (Figure 6). This allows saving a significant fraction of the chip area, and thereby increasing the pixel density. Based on the current stimulation thresholds, and on a computational model of the photovoltaic pixels[7], we project that pixel size can be decreased to 40μm. Therefore, in addition to 70μm pixels, we are producing 55 and 40μm pixels using this technology

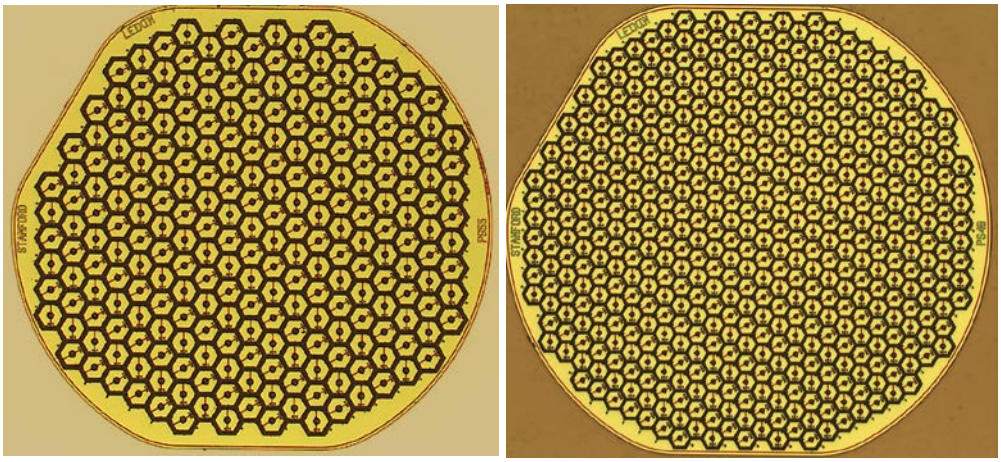

Figure 5. By eliminating the open trenches surrounding the pixels, reducing the width of the isolating trenches from 5 to 1 μm, and decreasing the size of the diodes, we reduced pixel pitch from 75μm to 55 and 40 μm. This enables placement of more than 10,000 pixels within 20° of the visual field.

(Figure 5). It provides more than 10,000 pixels within 20 degrees of the visual field in a human eye, and may enable spatial resolution corresponding to 20/120 visual acuity. If successful, this would make photovoltaic implants applicable not only to RP patients, but also to much larger population of the visually impaired, including millions of people with loss of central vision due to geographic atrophy.

More compact design of the 55μm pixels provides similar photodiode area to the current 70μm pixels. Pixels of 40μm in width (Figure 5) have twice smaller photodiode area, but, since the current stimulation thresholds (0.33 mW/mm^2, 10 ms) are much lower than the safety limits, we can afford doubling the light intensity. More limiting factor in this case becomes the size of the active electrode rather than photodiode area. Currently, with 70μm pixels, the active electrode is 18μm in diameter[1]. With 55 μm pixels, it is decreased to 14μm, and in 40 μm pixels – to 10μm. According to computational modelling of the photovoltaic pixel[7], we should be able to stimulate retinal neurons using 40μm pixels (twice smaller photodiode area and 3.3 times smaller electrode area than in the current 70 μm pixels) while staying below the 5 mW/mm^2 light intensity, planned to be the maximum irradiance in the goggle projection system for human use[6].

In addition to NIR light intensity, two additional factors limit the stimulation thresholds: size of the stimulating electrodes and proximity to the target neurons[8]. We are improving both factors by adding the third dimension to electrodes using electroplated pillar electrodes. We demonstrated retinal migration into 3-D implants several years ago[9], and proposed the concept of pillar electrodes to improve proximity to the inner retinal neurons. Trying to implement them, we explored multiple fabrication technologies, but integration of the conductive pillars with photodiode arrays was elusive until now. We developed electroplating and 3-D lithography that enabled fabrication of conductive pillars on top of the active electrodes, and SIROF deposition on top of them as well as on the return electrodes at the base of the pixels. Electroplating enables not only control of the pillar height, but also creating the hemispherical top, which doubles the surface area, compared to a flat disk of the same diameter. Example of the electroplated pillar with rounded top is shown in Figure 8.

Electroplating is fully compatible with the rest of the fabrication process, and allows several

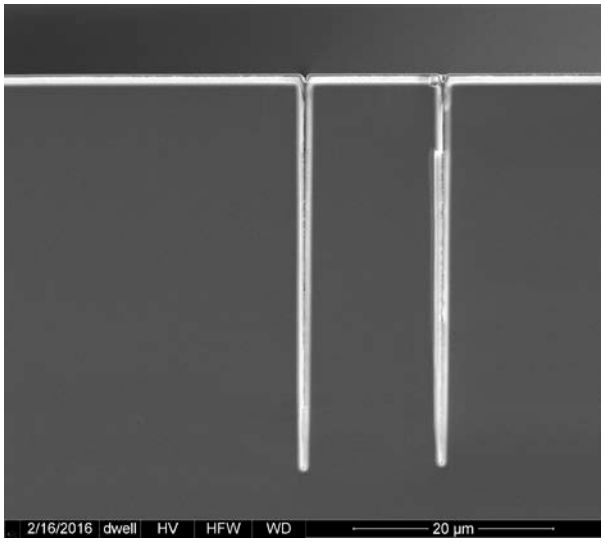

Figure 6: Two trenches of 1μm in width and 45 μm in depth etched in silicon wafer and filled with thermal oxide.

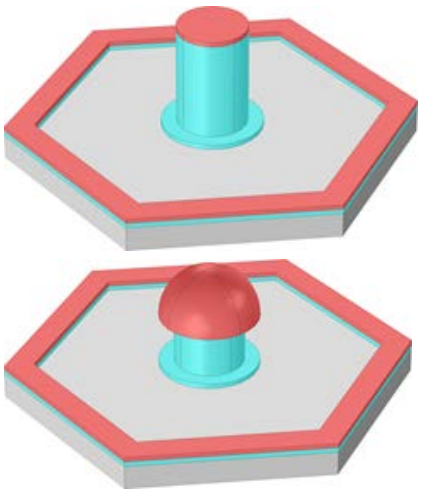

Figure 7. Pillar electrodes with flat top and with a hemispherical dome (bottom). Electrodes are coated with SIROF (red).

Figure 8. Electroplated electrodes with 10μm wide pillars and rounded tops.

additional beneficial features. To provide overlap of the sacrificial layer of metal which conducts current to the electrodes during electroplating, we start with pillars of smaller diameter than the active electrodes. With vertical pillars, it results in the top electrode been smaller than the active electrode at the base of the pixel, as shown in Figure 7A. However, we can expand the electrodes by adding a wider cap, as shown in Figure 7B and 8. Hemispherical caps have twice larger surface area than flat disks of the same diameter, thereby increasing the maximum injectable charge from the active electrodes. In addition, hemispherical tops eliminate sharp corners on the flat pillars, which sometimes catch the retina during implantation.

To provide sufficient capacitance, both active and return electrodes in our arrays are coated with sputtered iridium oxide (SIROF)[10]. This material has proven efficient for retinal stimulation and stable during a year-long follow-up in-vivo [1]. Capacitance of this material is on the order of 1 mF/cm^2 [7] – two orders of magnitude larger than that of polished metal electrodes in electrolyte (10 μF/cm^2), and about an order of magnitude larger than that of Pt grey (~100 μF/cm^2). Due to much larger capacitance of this coating, current is ejected primarily from the coated top of the pillar, rather than from its flat Pt side walls[11]. This effect eliminates the need for insulation of the side walls, thereby greatly simplifying the fabrication process.

Major Tasks 3 and 4: Development of the NIR video goggles, Development of the image processing software and user interface

The first iteration of the video goggles produced by Pixium Vision (French company commercializing our implants) for AMD patients blocks both eyes. Images captured by the camera are projected onto the retina using pulsed near-infrared (880nm) light. These goggles are now used for evaluation of prosthetic vision, including spatial resolution, number of levels of grey, usefulness for reading, face recognition, and other tasks of daily living. The second iteration will be monocular: the better eye will not be obstructed, while the implanted eye will be presented with images for only prosthetic part of the visual field, while its peripheral field is blocked. We expect the perceptual merger of two different images in two eyes work similarly to that in presbiopic patients wearing two different contact lenses optimized for the near and far distances. We will assess perceptual integration of such vision on various static images and with video.

AMD patients lose central vision, but retain normal peripheral vision. Therefore, ultimate video goggles activating retinal implants in the macula with NIR light should not obstruct peripheral vision. To assess perceptual integration of prosthetic and natural vision, we developed software for augmented-reality goggles (ODG) and simulation on a laptop computer using eye tracking (Tobii). We will also use them for assessment of the effects of the image processing on perception of the low resolution and low dynamic range images.

Using rapid eye tracking (90 Hz, Tobii), we created an image processing app to simulate scotoma of arbitrary shape and location in the visual field by blocking (graying-out) visual information in this area. Rapid eye tracking will ensure that the “scotoma” always stays on the same part of the retina. By adjusting the size and shape of this artificial scotoma, we evaluate the residual visual acuity in various retinal conditions, such as the loss of central vision in AMD, peripheral vision in retinitis pigmentosa and glaucoma, or irregular scotomata in cases of retinal trauma.

Benefits of the image processing for enhancement of prosthetic vision within the limitations of pixel size, dynamic range, and others, may include electronic zoom, contrast enhancement, edge enhancement, image sparsity, contrast reversal, image stabilization for reading, and other functions.

Reduced contrast sensitivity significantly affects perception of natural scenes. Due to adaptation to the average luminance, local spatio-temporal contrast of a visual stimulus defines visual perception of brightness [12-14]. In humans, the eyes typically fixate for 200-300 ms, and the retina locally adapts to the average luminance [15, 16]. Upon ocular movement to another position (such as microsaccades, drift, and ocular tremor), the image on the retina shifts and retinal ganglion cells respond to the local change in contrast [17]. Both, the implant pixel size and contrast sensitivity provided by the device will therefore impact the patient's ability to perceive images. We illustrated this effect using sinusoidal gratings of various spatial frequencies and contrasts, shown in circular patches corresponding to 2º of visual angle (Figure 9). An image sampled by retinal prosthesis becomes pixelated, as shown in Figure 9 B-D. For natural spatial resolution, local contrast within each patch remains relatively constant across spatial frequencies (Figure 9A). Areas with maximum local contrast (MLC) exceeding 1% are below the green line. Pixilation in prosthetic vision reduces both, spatial resolution and contrast of the high-density patterns. For example, arrays with 40µm pixels can resolve patches below 2 cpd (150 µm/cycle), while they are unable to properly sample above 8 cpd (37.5 µm/cycle). Intermediate spatial frequencies create heavy aliasing, as exemplified in the patch of 4 cpd at the bottom of Figure 9C. Decrease in pixel size not only improves spatial resolution, but also increases the average local contrast, as illustrated by the 3 lines outlining the areas of local contrast exceeding 1, 12 and 20%.

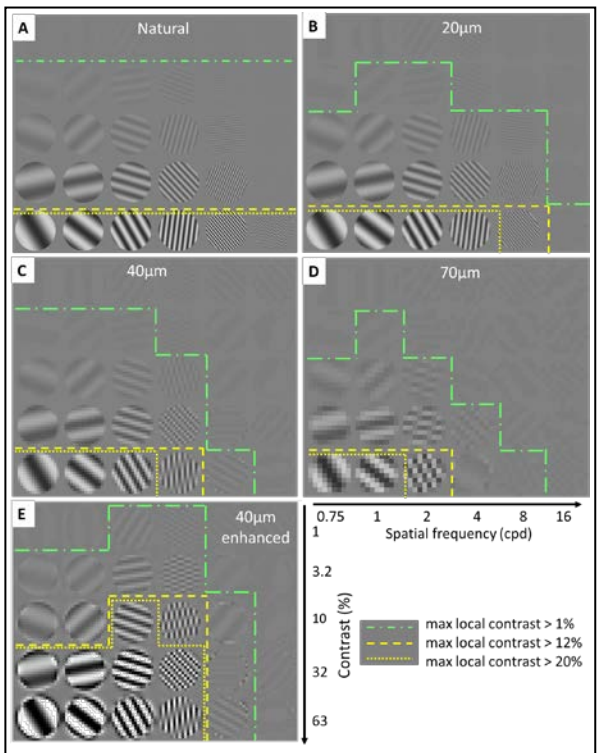

Figure 9. Mimicking integration of prosthetic and natural vision. Grey area illustrates scotoma in AMD patient, partially filled with prosthetic image composed of 2000 pixels at 8 grey levels.

Image processing prior to projection onto the photovoltaic array can help improve the contrast of a pixelated image. For example, application of unsharp masking enhances the 40µm-pixelated image, as illustrated in Figure 9E: with sharpened edges and increased dynamic range, local contrast is increased. This increases the areas visible within the limited contrast sensitivity of prosthetic vision, as outlined by the yellow dash lines. Without image processing, prosthetic vision can only identify 3-4 patches (63% contrast, < 4cpd). In the enhanced image, 6 additional patches exceed the contrast sensitivity threshold of prosthetic vision (>10% original contrast).

We will continue exploring various image processing algorithms on perception of the pixelated images with lower dynamic range, including contrast enhancement, edge enhancement, image sparsity, electronic zoom, contrast reversal, image stabilization, and others. In particular, we will evaluate object recognition tasks, such as reading speed and identification of simple objects [18].

Key Research Accomplishments

- We developed the SiC protective coating demonstrated its stability, biocompatibility and excellent protection of the photovoltaic retinal prosthesis in-vitro and in-vivo.
- We optimized the configuration of return electrodes in neurostimulating arrays for high resolution retinal stimulation, and demonstrated that boundary condition in steady state corresponds to constant current density, which is very important for proper computational modeling of electric field in tissue.
- We demonstrated that prosthetic visual responses in rat retina exhibit antagonistic center-surround organization with receptive field sizes very similar to natural.
- We demonstrated that temporal structure in spiking patterns of ganglion cells defines perceptual thresholds in rodents with subretinal prosthesis, and that contrast sensitivity of prosthetic vision is about 6 times lower than natural.
- We produced subretinal photovoltaic arrays with pixels of 40 and 55um in size and pillar electrodes, and are working now on evaluation of the retinal responses to 3-D electro-neural interfaces.
- We transferred the technology of photovoltaic arrays to Pixium Vision – a company that commercializes this technology. A few months ago, Pixium Vision started the first clinical trial and demonstrated that 2x2 mm photovoltaic array (PRIMA) can be safely implanted under the atrophic macula and restore central visual perception in patients with dry-AMD, with resolution up to the limits of the implant.

Reportable Outcomes

Refereed publications:

- Optimization of Pillar Electrodes in Subretinal Prosthesis for Enhanced Proximity to Target Neurons. T Flores, X. Lei, T. Huang, H. Lorach, R. Dalal, L. Galambos, T. Kamins, K. Mathieson and D. Palanker. *J. Neural Eng*. **15** 036011 (13pp) (2018).
- Temporal Structure in Spiking Patterns of Ganglion Cells Defines Perceptual Thresholds in Rodents with Subretinal Prosthesis. E. Ho, H. Lorach, G. Goetz, F. Laszlo, X. Lei, T. Kamins, J.C. Mariani, A. Sher, and D. Palanker. *Scientific Reports* **8**:3145 (2018).
- Spatio-temporal Characteristics of Retinal Response to Network-mediated Photovoltaic Stimulation. E. Ho, R. Smith, G.A. Goetz, X. Lei, L. Galambos, T.I. Kamins, J. Harris, K. Mathieson, D. Palanker, A. Sher. *Journal of Neurophysiology* 18 October (2017)
- Electronic Approaches to Restoration of Sight. G. Goetz and D. Palanker. *Reports on Progress in Physics* **79:** 096701 (29pp) (2016)
- SiC protective Coating for Photovoltaic Retinal Prosthesis. X. Lei, S. Kane, S. Cogan, H. Lorach, L. Galambos, P. Huie, K. Mathieson, T. Kamins, J. Harris and D. Palanker. *Journal of Neural Engineering* **13**: 046016 (12pp) (2016).
- Optimization of Return Electrodes in Neurostimulating Arrays. T. Flores, G. Goetz, X. Lei, and D. Palanker. *Journal of Neural Engineering* **13**: 036010 (11pp) (2016).
- High Resolution Photovoltaic Subretinal Prosthesis for Restoration of Sight. H. Lorach and D. Palanker. Chapter 9 in "Artificial Vision: a Clinical Guide". P. Gabel (Editor). Springer International Publishing, 2016.
- Implantation of Modular Photovoltaic Subretinal Prosthesis. D.Y. Lee, H. Lorach, P. Huie, D. Palanker. *Ophthalmic Surgery, Lasers and Imaging Retina*. **47**: 171-174 (2016).
- Retinal Safety of Near Infrared Radiation in Photovoltaic Restoration of Sight. H. Lorach, J. Wang, D.Y. Lee, R. Dalal, P. Huie, D. Palanker. *Biomedical Optics Express* 7(1): 13-21 (2015).
- Interactions of Prosthetic and Natural Vision in Animals With Local Retinal Degeneration. H. Lorach; X. Lei; L. Galambos; T. Kamins; K. Mathieson; R. Dalal; P. Huie; J. Harris; D. Palanker. *Investigative Ophthalmology and Visual Science* 56: 7444-7450 (2015).
- Contrast Sensitivity with a Subretinal Prosthesis and Implications for Efficient Delivery of Visual Information. G. Goetz, R. Smith, Xin Lei, L. Galambos, T. Kamins, K. Mathieson, A. Sher, and D. Palanker. *Investigative Ophthalmology and Visual Science* 56: 7186–7194 (2015).
- Development of Animal Models of Local Retinal Degeneration. Henri Lorach, Jennifer Kung, Corinne Beier, Yossi Mandel, Roopa Dalal, Philip Huie, Jenny Wang, Seungjun Lee, Alexander Sher, Bryan William Jones, and Daniel Palanker. *Investigative Ophthalmology and Visual Science* 56(8): 4644-4652 (2015).
- Photovoltaic Restoration of Sight with High Visual Acuity. H. Lorach, G. Goetz, R. Smith, X. Lei, Y. Mandel, T. Kamins, K. Mathieson, P. Huie, J. Harris, A. Sher, and D. Palanker. *Nature Medicine*, **21**:476–482 (2015).

Conference presentations:

1. Photovoltaic restoration of sight in rodents with retinal degeneration. Daniel Palanker; SPIE, Photonics West, San Francisco, 2017
2. Photovoltaic restoration of sight in rodents with retinal degeneration. Henri Lorach, Dae-Yeoung Lee, Xin Lei, Roopa Dalal, Theodore Kamins, Ludwig Galambos, James Harris, Daniel Palanker; The Eye and The Chip. Biannual International Symposium on Artificial Vision. Detroit, 2017.
3. Photovoltaic Restoration of Sight: from Bench to Bedside. D. Palanker, H. Lorach, X. Lei, T. Kamins, J. Harris, K. Mathieson. The Eye and The Chip. Biannual International Symposium on Artificial Vision. Detroit, 2017.

4. Implications of low prosthetic contrast sensitivity for delivery of visual information. Georges Goetz, Richard Smith, Xin Lei, Ludwig Galambos, Theodore Kamins, Keith Mathieson, Alexander Sher, Daniel Palanker; ARVO 2016
5. Robert and Gerry Ligon Lectureship at Vision Research Center, Kresge Eye Institute, Detroit. May 2016 “Photovoltaic Restoration of Sight in Rodents with Retinal Degeneration”
6. Annual Meeting of the Israeli Society for Vision and Eye Research. Ramat Gan, March 2016; “Photovoltaic restoration of sight in animals with retinal degeneration”.
7. Photovoltaic restoration of sight in rodents with retinal degeneration. Daniel Palanker; SPIE, Photonics West, San Francisco, 2017
8. Photovoltaic restoration of sight in rodents with retinal degeneration. Henri Lorach, Dae-Yeoung Lee, Xin Lei, Roopa Dalal, Theodore Kamins, Ludwig Galambos, James Harris, Daniel Palanker; The Eye and The Chip. Biannual International Symposium on Artificial Vision. Detroit, 2017.
9. Photovoltaic Restoration of Sight: from Bench to Bedside. D. Palanker, H. Lorach, X. Lei, T. Kamins, J. Harris, K. Mathieson. The Eye and The Chip. Biannual International Symposium on Artificial Vision. Detroit, 2017.
10. Implications of low prosthetic contrast sensitivity for delivery of visual information. Georges Goetz, Richard Smith, Xin Lei, Ludwig Galambos, Theodore Kamins, Keith Mathieson, Alexander Sher, Daniel Palanker; ARVO 2016
11. Robert and Gerry Ligon Lectureship at Vision Research Center, Kresge Eye Institute, Detroit. May 2016 “Photovoltaic Restoration of Sight in Rodents with Retinal Degeneration”
12. Annual Meeting of the Israeli Society for Vision and Eye Research. Ramat Gan, March 2016; “Photovoltaic restoration of sight in animals with retinal degeneration”.

Conclusion

Ocular trauma can result in traumatic retinopathy, which, like retinal degeneration, leads to blindness due to loss of photoreceptors. Visual information can be reintroduced into the retina by patterned electrical stimulation of the remaining inner retinal neurons. Photovoltaic subretinal prosthesis directly converts light into pulsed electric current in each pixel, stimulating the nearby neurons. Images captured by the head-mounted camera are projected onto retina by video goggles using pulsed near-infrared (~880nm) light. We prepared this technology for clinical trial, including optimization of the photovoltaic array, addition of the biocompatible protective coating for long-term implantation in human patients, fabrication of the video goggles with a camera, and image processing software. In particular, we (1) Developed and tested the SiC protective biocompatible coating for the implant. (2) Optimized the pixel configuration to maximize its performance, including the light-to-current conversion, dynamic range, maximum repetition rate, minimum cross-talk and minimum pixel size. (3) Developed the near-infrared pulsed video goggles and image processing software.

After technology transfer to Pixium Vision, the first clinical trial started in early 2018. To date, 3 photovoltaic wireless chips (PRIMA) have been implanted in patients with central geographic atrophy. Implants are of 2x2mm in size, 30μm in thickness, containing 378 pixels of 100μm each. In all patients, the chip remained stable under the macula after implantation. All patients perceive white-yellow patterns with adjustable brightness, in retinotopically correct locations. Majority of patients correctly differentiate simple objects and recognize patterns, such as bars at different orientations, with spatial resolution up to the limits of the implant. These results indicate that further development of smaller pixels should provide higher resolution and enable even more functional restoration of sight.

References

1. Lorach, H., et al., *Photovoltaic restoration of sight with high visual acuity.* Nature Medicine, 2015. **21**(5): p. 476-82.
2. Goetz, G., et al., *Contrast Sensitivity With a Subretinal Prosthesis and Implications for Efficient Delivery of Visual Information.* Invest Ophthalmol Vis Sci, 2015. **56**(12): p. 7186-94.
3. Ho, E., et al., *Temporal structure in spiking patterns of ganglion cells defines perceptual thresholds in rodents with subretinal prosthesis.* Scientific Reports, 2018. **8**(1): p. 3145.
4. Mathieson, K., et al., *Photovoltaic retinal prosthesis with high pixel density.* Nature Photonics, 2012. **6**(6): p. 391-397.
5. Lei, X., et al., *SiC Protective Coating for Photovoltaic Retinal Prostheses.* Journal of Neural Engineering, 2016. **in review**.
6. Lorach, H., et al., *Retinal safety of near infrared radiation in photovoltaic restoration of sight.* Biomed Opt Express, 2016. **7**(1): p. 13-21.
7. Boinagrov, D., et al., *Photovoltaic Pixels for Neural Stimulation: Circuit Models and Performance.* IEEE Trans Biomed Circuits Syst, 2016. **10**(1): p. 85-97.
8. Palanker, D., et al., *Design of a High Resolution Optoelectronic Retinal Prosthesis.* Journal of Neural Engineering, 2005. **2**: p. S105–S120.
9. Butterwick, A., et al., *Effect of shape and coating of a subretinal prosthesis on its integration with the retina.* Exp Eye Res, 2009. **88**(1): p. 22-9.
10. Wang, L., et al., *Photovoltaic retinal prosthesis: implant fabrication and performance.* J Neural Eng, 2012. **9**(4): p. 046014.
11. Flores, T., et al., *Optimization of Return Electrodes in Neurostimulating Arrays.* Journal of Neural Engineering, 2016. **in print**.
12. Rucci, M. and J.D. Victor, *The unsteady eye: an information-processing stage, not a bug.* Trends in neurosciences, 2015. **38**(4): p. 195-206.
13. Shapley, R. and C. Enroth-Cugell, *Visual adaptation and retinal gain controls.* Progress in retinal research, 1984. **3**: p. 263-346.
14. Shapley, R., E. Kaplan, and K. Purpura, *Contrast sensitivity and light adaptation in photoreceptors or in the retinal network.* Contrast sensitivity, 1993. **5**: p. 103-116.
15. Shapley, R., *Retinal physiology: adapting to the changing scene.* Curr Biol, 1997. **7**(7): p. R421-3.
16. Troy, J.B. and C. Enroth-Cugell, *X and Y ganglion cells inform the cat's brain about contrast in the retinal image.* Experimental Brain Research, 1993. **93**(3): p. 383-90.
17. Baccus, S.A. and M. Meister, *Fast and slow contrast adaptation in retinal circuitry.* Neuron, 2002. **36**(5): p. 909-919.
18. Jung, J.H., et al., *Active confocal imaging for visual prostheses.* Vision Res, 2015. **111**(Pt B): p. 182-96.

Participants & other Collaborating Organizations

Organization Name: Stanford University

**Location of Organization: Hansen Experimental Physics Laboratory,
452 Lomita Mall, Astrophysics Building,
Room S05 & S04, Stanford, CA 94305-4085**

1. Prof. Daniel Palanker

Name:	Daniel Palanker
Project Role:	PI
Nearest person month worked:	2.4 CM
Contribution to Project:	Directs the project, evaluates the results, writes the reports and publications.

2. Mr. Yi Quan

Name:	Yi Quan
Project Role:	Research Associate
Nearest person month worked:	2.4 CM
Contribution to Project:	Helps with animal protocols, tissue processing and immunohistochemistry.

3. Mr. Ludwig Galambos

Name:	Ludwig Galambos
Project Role:	Research Associate/Engineer
Nearest person month worked:	3.0 CM
Contribution to Project:	Works on fabrication of the photovoltaic arrays

4. Ms. Roopa Dalal

Name:	Roopa Dalal
Project Role:	Research Associate (Histologist)
Nearest person month worked:	1.0 CM
Contribution to Project:	Works on tissue fixation, embedding, histological sectioning, staining and microphotography.

5. Ms. Xin Lei

Name:	Xin Lei
Project Role:	Graduate Student
Nearest person month worked:	3.0 CM
Contribution to Project:	Works on design and fabrication of the photovoltaic arrays.

6. Mr. Thomas Flores

Name:	Tom Flores
Project Role:	Graduate Student
Nearest person month worked:	3.0 CM
Contribution to Project:	Works on design and fabrication of the photovoltaic arrays.

7. Mr. Henri Charles Lorach

Name:	Henri Charles Lorach
Project Role:	Senior Science Research Assoc
Nearest person month worked:	3.0 CM
Contribution to Project:	Works on all the aspects of the project related to animal models of retinal degeneration & animal surgery